Diblock Copolymer Thin Films: A Field-Theoretic Simulation Study

Alfredo Alexander-Katz[†,‡,*] and Glenn H. Fredrickson[§,||]

Physics Department, Technical University of Munich, D-80538, Garching, Germany, and Department of Physics, Department of Chemical Engineering, and Materials Research Laboratory, University of California, Santa Barbara, California 93106

Received January 2, 2007; Revised Manuscript Received March 19, 2007

ABSTRACT: Using field-theoretic simulations, we study a symmetric diblock copolymer melt confined between two parallel neutral walls separated by a distance L. We consider two scenarios: a mean-field regime and a fluctuating case corresponding to a polymerization index $N \sim 10^5$. For both cases, we analyze the behavior of this system in the disordered and the ordered phases as a function of the film thickness L. In particular, we compute the structure factor for each case, and compare it to the predicted structure factor for a bulk system using the random phase approximation. In the disordered phase, we find qualitative agreement with the bulk system, except that the amplitudes are dependent on the modes perpendicular to the slit. The ordered structure in all cases was found to be a lamellar phase oriented perpendicular to the walls. Also, we studied the location of the order−disorder transition (ODT) in both cases. In the mean-field regime, it was found that the transition is insensitive to the width of the cavity, and occurs, as expected, at $\chi N^* = 10.5$. For the fluctuating case, we find a shift in the ODT that becomes essentially constant for slit widths larger than the unperturbed radius of gyration of the copolymers. For thicknesses below this value, we observe a confinement induced melting of the film, for which a theoretical explanation is proposed.

I. Introduction

Block copolymers are polymer chains comprised of two (or more) chemically distinct segments covalently bonded at one (or both) ends. An attractive feature of these polymers is that they can self-assemble into ordered structures[1,2] with dimensions of the order of the size of the copolymers themselves, i.e., 5−50 nm. This desirable feature has made them a prime candidate for technological applications, such as nanolithography, thermoplastic elastomers, pressure sensitive adhesives, and high-density storage media, to name a few.[3−7] Many of the emerging applications require the polymers to be constrained to a film, or to some other confining cavity.[8] As a result, there has been a surge of experimental[9−18] and theoretical[19−27] research in block copolymer thin films. Much of the research in this area has focused on the different phases that appear in thin film environments, as well as on devising ways to control the surface orientation of different morphologies, but there have been only a few works where the effect of confinement on fluctuations and the order−disorder transition (ODT) has been studied. Also, most theoretical studies have relied on the mean-field approximation embodied in self-consistent field theory (SCFT)[28] which is known to break down in the vicinity of the ODT.

From the standpoint of computer simulations, several groups have studied block copolymers using particle-based simulations in the bulk.[29,30] Although no approximation is invoked in these studies, the limited range of densities and chain lengths that can be accessed have so far yielded results that are different from those calculated analytically[31,32] and studied experimentally.[33] In particular, the particle-based simulations in the case of a symmetric diblock found an ODT temperature independent of N and considerably lower than that found using field-based theories. In contrast, field-theoretic computer simulations (FTS) invoke the same underlying statistical field theory models used in analytical calculations and are advantaged over particle-based simulations at melt densities and high molecular weight.[34,35] Such simulations have been used to study the bulk ODT of diblock copolymers,[36] but they have not yet been applied to study the ordering behavior of confined block copolymer films. In the case of polymer films, most computational studies have focused on the orientation of the micro structures due to confinement, as well as preferential interactions with the walls.[19,22−26,37,38]

In this paper we present results from FTS simulations on the ordering behavior of confined symmetric diblock copolymer melts. We consider the melt to be confined between two parallel neutral surfaces that do not exert any preferential attraction on either type of polymer segment. Although typically one segment species has a preferential affinity at both solid and vapor boundaries, it is desirable to understand the effect of pure confinement on composition fluctuations and ordering. Moreover, it has been shown experimentally that by use of random copolymers it is feasible to construct neutral surfaces.[39] Past theoretical studies on symmetric diblock melts confined by neutral surfaces have primarily focused on understanding the orientation of the lamellar mesophase as a function of the width of the slit, since there was a dispute in the literature concerning whether the lamellae orient perpendicular, or parallel to the confining surfaces. The consensus opinion from SCFT calculations is that the perpendicular morphology is stable for diblock films confined by two neutral surfaces at all film thicknesses,[19,40,41] a result also consistent with the present work.

Beyond mean-field theory, there is very little theoretical or computer simulation work on confined block copolymer films that studies the effects of confinement on the order−disorder transition (ODT). The first work in this direction was performed by Milner and Morse,[20] where they used the Brazovskii approximation[42] to study the transition of confined symmetric diblock copolymers. In particular, they were interested in the behavior of diblocks orienting parallel to the walls with and

† Physics Department, Technical University of Munich.
‡ Department of Physics, University of California, Santa Barbara.
§ Department of Chemical Engineering, University of California, Santa Barbara.
|| Materials Research Laboratory, University of California, Santa Barbara.

10.1021/ma070005h CCC: $37.00
Published on Web 04/28/2007

without surface interactions. They found a width dependent ODT temperature in the case of neutral surfaces, but the analysis did not include the perpendicular orientation, which as explained before is believed to be the stable orientation under these conditions. More recently, a particle-based simulation[43] was used to study the effect of confinement on the order−disorder transition of a triblock copolymer melt under lamellae forming conditions. The particular findings of this work were that the ODT temperature becomes constant once the film thickness is above $\sim 3R_{go}$ (R_{go} is the unperturbed copolymer radius of gyration), a width comparable to the lamellar period, and increases quite abruptly below this value. During the preparation of this manuscript, a new article by Shi and co-workers was published in which they reanalyzed the confined symmetric diblock system using the Brazovskii analysis and a Gaussian treatment of fluctuations.[27] In this work they report that thin films oriented perpendicularly become unstable for film thicknesses below $\sim 1.5R_{go}$, a finding close to that found in the present work, where we study the same system using full FTS simulations. Our simulations have the advantage of not relying on the analytical approximations invoked by Shi and co-workers.

This article is organized in the following way: in section II, we provide the theoretical background on the field-theoretic formulation of a diblock copolymer melt, and introduce the observable quantities that will be studied in the subsequent parts of the paper. In section III, we describe the numerical methods employed in the FTS simulations. Section IV contains our simulation results for a confined symmetric diblock film. In particular, we present and discuss the structure factor as a function of film thicknesses in the disordered and ordered phases. We finish the section with a phase diagram in the coordinates of film thickness and block incompatibility χN. Last, section V contains some concluding remarks.

II. Formalism

A. Field Theory Model. In this section we present the diblock copolymer model that will be used in subsequent parts of this paper. Specifically, we invoke the "standard'' field theory model of an incompressible AB diblock copolymer melt.[44] This model treats individual diblock copolymers in the continuous Gaussian chain description, includes a Flory-type contact interaction χ among dissimilar block segments (A and B), and constrains the total segment number density to a constant value ρ_0 at all points r in the system volume V. The block copolymers are assumed to be monodisperse with a total of N statistical segments; N_A segments of type A and $N_B = N - N_A$ segments of type B. Statistical segments are assumed to occupy equal volumes $v = 1/\rho_0$ and have equal segment lengths b. The average volume fraction of type A segments in the copolymer is denoted by $f = N_A/N$.

Through the use of Hubbard−Stratonovich−Edwards transforms, the segmental interactions in the above model can be decoupled with two auxiliary fields. Upon tracing out the chain coordinates, the nVT canonical partition function can be reexpressed as an interacting (classical) statistical field theory. We refer the interested reader to the literature for the details of this derivation,[34,35,44] and simply report the final result here. Specifically, the partition function for n diblock chains in a volume V can be expressed as

$$Z \propto \int \mathcal{D}\omega_- \int \mathcal{D}\omega_+ \exp(-H[\omega_+,\omega_-]) \tag{1}$$

where the effective Hamiltonian is given by

$$H[\omega_+,\omega_-] = -n \ln Q[\omega_+,\omega_-] - i\rho_o \int d\mathbf{r}\, \omega_+(\mathbf{r}) + \frac{\rho_o}{\chi}\int d\mathbf{r}\, \omega_-{}^2(\mathbf{r}) \tag{2}$$

The functional $Q[\omega_+,\omega_-]$ corresponds to the partition function of a single polymer in the auxiliary fields $i\omega_+$ (purely imaginary) and ω_- (purely real), where $i \equiv \sqrt{-1}$. The two fields have different roles in the theory: ω_+ can be interpreted as a fluctuating pressure that enforces incompressibility, while ω_- is an exchange potential that defines the fluctuating composition profile in the AB copolymer melt. In particular, the latter field is conjugate to the local density difference between A and B defined as

$$\hat{\rho}_-(\mathbf{r}) = \hat{\rho}_A(\mathbf{r}) - \hat{\rho}_B(\mathbf{r}), \tag{3}$$

where $\hat{\rho}_A(\mathbf{r})$ and $\hat{\rho}_B(\mathbf{r})$ are the local density operators of the A and B type of monomers respectively.

The single polymer partition function $Q[\omega_+,\omega_-]$ can be evaluated in the usual way[34,35,44]

$$Q[\omega_+,\omega_-] = \frac{1}{V}\int d\mathbf{r}\, q(\mathbf{r}, N; [\omega_+,\omega_-]), \tag{4}$$

where the function $q(\mathbf{r}, N; [\omega_+,\omega_-])$ is a propagator that describes the probability of observing the Nth segment of the chain at position $\mathbf{r}$, given all possible placements of the first segment. This propagator satisfies the following modified diffusion equation

$$\frac{\partial}{\partial s} q(\mathbf{r}, s; [\omega]) = \frac{b^2}{6}\nabla^2 q(\mathbf{r}, s; [\omega]) - \omega(\mathbf{r}, s)\, q(\mathbf{r}, s; [\omega]), \tag{5}$$

with the initial condition

$$q(\mathbf{r}, 0; [\omega]) = 1 \tag{6}$$

and the s-dependent field $\omega(\mathbf{r}, s)$ defined by

$$\omega(\mathbf{r}, s) = \begin{cases} i\omega_+(\mathbf{r}) - \omega_-(\mathbf{r}) & \text{if } 0 < s \le fN \\ i\omega_+(\mathbf{r}) + \omega_-(\mathrm{r}) & \text{if } fN < s \le N \end{cases} \tag{7}$$

At this point, it is desirable to express the theory in dimensionless form. A convenient choice is to scale all lengths by the unperturbed radius of gyration $R_{go} = b\sqrt{N/6}$, and to scale curvilinear displacements s along the chain contour by N. Using the rescaled quantities, the partition function can be rewritten as

$$Z \propto \int \mathcal{D}\Omega_+ \int \mathcal{D}\Omega_- \, e^{-H[\Omega_+,\Omega_-]} \tag{8}$$

with rescaled fields $\Omega_\pm = N\omega_\pm$, and the action H now given by

$$H[\Omega_+,\Omega_-] = -C\left\{V \ln Q[\Omega_+,\Omega_-] + i\int d\mathbf{r}\, \Omega_+(\mathbf{r}) - \frac{1}{\chi N}\int d\mathbf{r}\, [\Omega_-(\mathbf{r})]^2\right\} \tag{9}$$

with $C \equiv \rho_0 R_{go}{}^3/N$. As before, the single diblock partition function $Q[\Omega_+,\Omega_-]$ is given by

$$Q[\Omega_+,\Omega_-] = \frac{1}{V}\int d\mathbf{r}\, q(\mathbf{r}, 1; [\Omega_+,\Omega_-]) \tag{10}$$

where the function $q(\mathbf{r}, s; [\Omega_+,\Omega_-])$ now satisfies

$$\frac{\partial}{\partial s}q(\mathbf{r}, s; [\Omega]) = \nabla^2 q(\mathbf{r}, s; [\Omega]) - \Omega(\mathbf{r}, s)q(\mathbf{r}, s; [\Omega]) \tag{11}$$

with the initial condition

$$q(\mathbf{r}, 0; [\Omega]) = 1 \tag{12}$$

and the field $\Omega(\mathbf{r}, s)$ defined as

$$\Omega = \begin{cases} i\Omega_+(\mathbf{r}) - \Omega_-(\mathbf{r}) & \text{if } 0 < s \le f, \\ i\Omega_+(\mathbf{r}) + \Omega_-(\mathbf{r}) & \text{if } f < s \le 1 \end{cases} \tag{13}$$

At fixed f (we shall subsequently be considering only the case of symmetric diblocks with $f = {}^1/_2$), and notwithstanding the size and shape of the computational cell, it is important to note that the rescaled field theory contains only two dimensionless parameters: χN and C. The block incompatibility parameter χN appears in the well-known mean-field theories of diblock copolymers,[31,44] while the dimensionless polymer concentration C reflects the average number of other copolymers that penetrate the coil of a test chain in the melt. As such, C is an effective coordination number that multiplies all terms in H and can be used as a Ginzburg parameter. The C parameter controls the departures from mean-field behavior in the sense that the mean-field approximation (SCFT) is exact for $C \to \infty$.

B. Observables. Density Operators. Within the FTS framework, observable quantities need to be expressed as *operators* that make the functional dependence on the fluctuating auxiliary fields explicit. Averages of these operators over an ensemble with the complex statistical weight $\exp(-H)$ produce ensemble-averaged real observables that can be compared with experimental measurements, theoretical calculations, or results from traditional particle-based simulations. Expressions for the reduced segment densities (volume fractions) in a block copolymer melt are well-known.[34,35] In particular, the reduced densities of A and B segments can be shown to be given by

$$\begin{aligned} \phi_A(\mathbf{r}; [\Omega_+,\Omega_-]) &= \frac{\rho_A(\mathbf{r}; [\Omega_+,\Omega_-])}{\rho_o} \\ &= \frac{1}{Q}\int_0^f \mathrm{d}s\, q^\dagger(\mathbf{r}, 1-s; [\Omega_+,\Omega_-])\, q(\mathbf{r}, s; [\Omega_+,\Omega_-]) \\ \phi_B(\mathbf{r}; [\Omega_+,\Omega_-]) &= \frac{\rho_B(\mathbf{r}; [\Omega_+,\Omega_-])}{\rho_o} \\ &= \frac{1}{Q}\int_1^f \mathrm{d}s\, q^\dagger(\mathbf{r}, 1-s; [\Omega_+,\Omega_-])\, q(\mathbf{r}, s; [\Omega_+,\Omega_-]) \end{aligned} \tag{14}$$

where f is as before the average volume fraction of type A segments, $f = N_A/N$. The single diblock partition function Q and the propagator $q(\mathbf{r}, s; [\Omega_+,\Omega_-])$ are given by eqs 10 and 11, respectively. In the final expressions we have also introduced a complementary propagator $q^\dagger(\mathbf{r}, s; [\Omega_+,\Omega_-])$, which is analogous to $q(\mathbf{r}, s; [\Omega_+,\Omega_-])$, but the propagation along the chain starts from the B end of the polymer. The $q^\dagger(\mathbf{r}, s; [\Omega_+,\Omega_-])$ propagator thus satisfies the following diffusion equation

$$\frac{\partial}{\partial s}q^\dagger(\mathbf{r}, s; [\Omega]) = \nabla^2 q^\dagger(\mathbf{r}, s; [\Omega]) - \Omega(\mathbf{r}, s)\, q^\dagger(\mathbf{r}, s; [\Omega]) \tag{15}$$

with the initial condition

$$q(\mathbf{r}, 0; [\Omega]) = 1 \tag{16}$$

and the field $\Omega(\mathbf{r}, s)$ is now given by

$$\Omega(\mathbf{r}, s) = \begin{cases} i\Omega_+(\mathbf{r}) + \Omega_-(\mathbf{r}) & \text{if } 0 < s \le 1-f, \\ i\Omega_+(\mathbf{r}) - \Omega_-(\mathbf{r}) & \text{if } 1-f < s \le 1 \end{cases} \tag{17}$$

Structure Factor. An important observable for the present work is the structure factor $S(\mathbf{k})$ because it gives information about the underlying correlations of segment density in the sample. Also, it is accessible in small-angle X-ray and neutron scattering experiments.[45,46] We will be particularly interested in the composition difference structure factor

$$S(\mathbf{k}) = \langle \hat{\rho}_-(\mathbf{k})\hat{\rho}_-(-\mathbf{k})\rangle \propto \langle \Omega_-(\mathbf{k})\Omega_-(-\mathbf{k})\rangle \tag{18}$$

where $\hat{\rho}_-(\mathbf{k}) = \hat{\rho}_A(\mathbf{k}) - \hat{\rho}_B(\mathbf{k})$ is the difference in the Fourier coefficients of the microscopic A and B segment densities defined in eq 3, and $\Omega_-(\mathbf{k})$ is the Fourier coefficient of the exchange field $\Omega_-(\mathbf{r})$ with wavevector $\mathbf{k}$. The final proportionality can be shown to be an exact relationship.[34,35] As will be discussed in the next section, we impose periodic boundary conditions in the plane of the film and Neumann (reflecting) conditions along the film normal (thickness direction z). The relevant Fourier basis functions are thus products of 2d plane waves and cosines, $\sim \exp(i\mathbf{k}_\rho\cdot\mathbf{r}_\rho)\cos(k_z z)$. The allowed wavevectors $\mathbf{k} = (\mathbf{k}_\rho, k_z)$ correspond to $k_z = \pi n_z/L$ along the film normal with nonnegative integer n_z (L is the film thickness), and to $k_{\rho j} = 2\pi n_j/L_\rho$ with integer n_j for each in-plane component $j = 1, 2$ of $\mathbf{k}_\rho$ (L_ρ is the lateral system size).

To study the order−disorder transition, we employ a quantity Ψ defined as

$$\Psi = \frac{1}{V^2}\sum_{\mathbf{k}} \langle \Omega(\mathbf{k})\Omega(-\mathbf{k})\rangle^2 \tag{19}$$

which displays a jump when one goes through the ODT. A related quantity was originally introduced by Vassiliev and Matsen[30] to locate the ODT for a symmetric diblock copolymer melt in a bulk simulation. In that work they used a real-space version of the formula presented above (apart from a χN dependent normalization). Since we are not interested in the actual value of the function, but rather on the location of the "discontinuity", eq 19 will suffice for our purposes. Our results using the formula presented above are shown at the end of this work, and display a jump of at least an order of magnitude in the value of Ψ as one crosses the ODT. The fact that one has gone through the disordering (or ordering) transition is corroborated by directly inspecting the structure factor.

III. Numerical Methods

In order to numerically sample the functional integral given by eq 8, we employ a real Langevin scheme. Given the fact that the Hamiltonian is in general complex, we separate the functional integrals defining the partition function as follows

$$Z \propto \int \mathscr{D}\Omega_-\, Z[\Omega_-] \exp\left(-\frac{C}{\chi N}\int \mathrm{d}\mathbf{r}\, [\Omega_-(\mathbf{r})]^2\right) \tag{20}$$

where $Z[\Omega_-]$ corresponds to

$$Z[\Omega_-] = \int \mathscr{D}\Omega_+ \exp(CV \ln Q[\Omega_+,\Omega_-] + iC\int \mathrm{d}\mathbf{r}\, \Omega_+(\mathbf{r})) \tag{21}$$

As can be seen, the complex nature of the Boltzmann weight is restricted to the functional $Z[\Omega_-]$. For large values of C (high molecular weight and high density), we expect that this functional integral will be dominated by the "partial saddle point'' with respect to the Ω_+ field.[35,47] With this assumption, we replace $Z[\Omega_-]$ by the mean-field "partition function'' $Z^*[\Omega_-]$, which is simply given by

$$Z^*[\Omega_-] = \exp\left(CV \ln Q[\Omega_+^*,\Omega_-] + iC\int d\mathbf{r}\, \Omega_+^*(\mathbf{r})\right) \quad (22)$$

where Ω_+^* satisfies the partial saddle point condition

$$\left.\frac{\delta H}{\delta \Omega_+}\right|_{\Omega_+{}^*} = 0 \quad (23)$$

at some fixed value of Ω_-. The following approximate expression for the partition function immediately results:

$$Z \approx \int \mathcal{D}\Omega_-\, Z^*[\Omega_-] \exp\left(-\frac{C}{\chi N}\int d\mathbf{r}\,[\Omega_-(\mathbf{r})]^2\right) \quad (24)$$

It can be shown that the partial saddle point solution Ω_+^* is purely imaginary, and thus by using this approximation we have effectively removed the imaginary part of the Hamiltonian, and hence eliminated the so-called "sign problem.'' As a consequence, a simple real Langevin scheme is suitable for sampling the fluctuations in the Ω_- field. The partial saddle point approximation we have just employed amounts to a constraint that the reduced total monomer density operator (which is averaged over all polymer configurations) is constant and equal to 1, or in other words $\phi_+(\mathbf{r}) = \phi_A(\mathbf{r}) + \phi_B(\mathbf{r}) = 1$, where the reduced densities $\phi_{A/B}$ are given by eq 14.[48] This approximation has been successfully used by Duchs et.al.[47] in their study of ternary blends, although they employ a different sampling algorithm in that work. An analysis of the validity of the approximation in the present context is given in Appendix A.

For the purpose of conducting FTS simulations, it is necessary to numerically sample eq 24 to generate a set of configurations of the Ω_- field distributed according to the probability distribution

$$P[\Omega_-] \propto \exp\left(\ln(Z^*[\Omega_-]) - \frac{C}{\chi N}\int d\mathbf{r}\,\Omega_-(\mathbf{r})^2\right) \quad (25)$$

As this is a positive semidefinite distribution, the sampling can be accomplished using familiar schemes such as Monte Carlo (MC), Langevin, or hybrid MC. Here, we adopt a simple Langevin scheme.

As usual, we discretize the theory on a uniform lattice and numerically simulate the lattice field theory. We summarize our algorithm in four steps as follows:

1. Initialize the $\Omega_{+/-}$ fields.
2. Evolve the Ω_- field one "time step'' by using a discrete Langevin update scheme.
3. Relax the Ω_+ field to its partial saddle-point solution Ω_+^* for the new Ω_- configuration.
4. Repeat steps 2 and 3 until the system has equilibrated and a sufficiently long Markov chain of field configurations has been achieved.

The initialization we use is to set both fields equal to zero, which is appropriate in order not to bias the morphology of the final state. The mean-field calculations are performed by considering a parameter $C \approx 20000$, which as will be shown later, suppresses fluctuations to an extent that mean-field solutions are generated.

In performing step 2, we use the following discrete Langevin update scheme

$$\Omega_-^{\mathrm{j}}(t+\Delta t) = \Omega_-^{\mathrm{j}}(t) - \Delta t\Gamma\frac{\partial H[\Omega_+^*,\Omega_-]}{\partial \Omega_-^{\mathrm{j}}(t)} + \sqrt{\Delta t}\eta^{\mathrm{j}}(t)$$

$$= \Omega_-^{\mathrm{j}}(t) - \Delta t\Gamma\Delta^3\mathbf{r}C\left(-\phi_-^{\mathrm{j}}(t;[\Omega_-,\Omega_+^*]) + \frac{2}{\chi N}\Omega_-^{\mathrm{j}}(t)\right) + \sqrt{\Delta t}\eta^{\mathrm{j}}(t) \quad (26)$$

where Ω_-^{j} and ϕ_-^{j} represent the value of the continuous field $\Omega_-(\mathbf{r})$ and continuous reduced density difference $\phi_-(\mathbf{r}) = \phi_A(\mathbf{r}) - \phi_B(\mathbf{r})$ at the cubic lattice site coordinates specified by the label $\mathrm{j} = (j_x,j_y,j_z)$. The lattice constants are Δx, Δy, and Δz in the x, y, and z directions, respectively, and the volume of a lattice site is denoted by $\Delta^3\mathbf{r} = \Delta x\Delta y\Delta z$. The factor $\Gamma > 0$ is a constant relaxation rate that is connected to the Langevin noise strength by a fluctuation−dissipation theorem. The field $\eta^{\mathrm{j}}(t)$ is a Gaussian real noise with first and second moments given by

$$\langle\eta^{\mathrm{j}}(t)\rangle = 0 \quad (27)$$

and

$$\langle\eta^{\mathrm{j}}(t)\eta^{\mathrm{j}'}(t')\rangle = 2\Gamma\delta_{\mathrm{j},\mathrm{j}'}\delta_{t,t'} \quad (28)$$

Step 3 is conducted with a simple explicit relaxation scheme, which we present here in its discrete version

$$\Omega_+^{\mathrm{j}}(t+\Delta t) = \Omega_+^{\mathrm{j}}(t) - \Delta t\frac{\partial H[\Omega_+,\Omega_-]}{\partial \Omega_+^{\mathrm{j}}}$$

$$= \Omega_+^{\mathrm{j}}(t) - \Delta t\Gamma\Delta^3\mathbf{r}\, iC(\phi_+^{\mathrm{j}}(t;[\Omega_-,\Omega_+]) - 1) \quad (29)$$

where as before Ω_+^{j} and ϕ_+^{j} represent the value of the continuous field $\Omega_+(\mathbf{r})$ and the continuous reduced total density $\phi_+(\mathbf{r}) = \phi_A(\mathbf{r}) + \phi_B(\mathbf{r})$ at the cubic lattice site coordinates specified by the label j. We relax Ω_+ according to this scheme until the variance of the reduced total density ϕ_+^{j} averaged over the lattice, $\sigma^2 = \langle(\phi_+^{\mathrm{j}})^2\rangle - \langle\phi_+^{\mathrm{j}}\rangle^2$, satisfies $\sigma^2 < 0.0001$, which implies that on average the local volume fraction is between 0.99 and 1.01 at each lattice point. A more sophisticated semi-implicit relaxation scheme for determining Ω_+^* was devised by Ceniceros and Fredrickson.[49] However, in the present application the number of relaxation steps required to update Ω_+^* from a solution at a previous time step is fairly small, i.e., about 5 iterations for each Ω_- field configuration, so both methods perform satisfactorily in our case.

All the simulations in this work were conducted on a $48 \times 48 \times n_z$ cubic lattice, with discretization $\Delta x = \Delta y = \Delta z = 0.25$ (in units of R_{go}), i.e. the lattice has dimensions $12R_{\mathrm{go}} \times 12R_{\mathrm{go}} \times L$. The value of n_z is determined by the thickness of the film as $n_z = L/\Delta z$. Periodic boundary conditions are applied on the $x-y$ directions, while we impose reflecting (Neumann) boundary conditions on both surfaces in the z direction. Previous studies[50,51] have shown that if one is not interested in the fluid structure within a correlation distance ξ from the walls over which the total segment density achieves its bulk value (ξ for a polymer melt is of order the segment size), reflecting boundary conditions provide a proper mesoscopic description of neutral surfaces. The diffusion equation was solved using a spectral collocation algorithm with a plane wave basis in the $x-y$ plane and a cosine basis along the slit normal z,[35,52,53] and the criteria

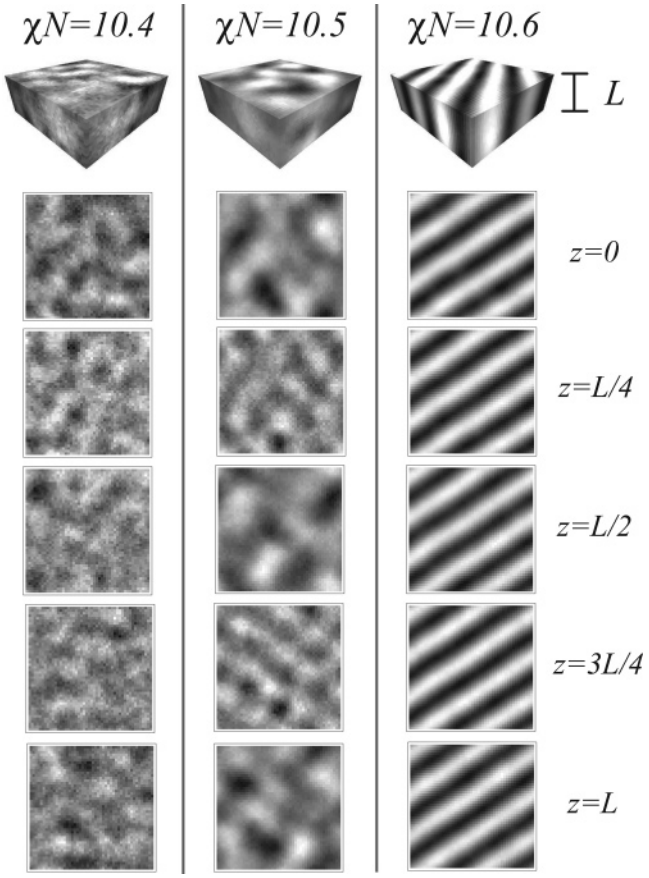

Figure 1. Snapshots of the instantaneous ϕ_- field at different layers corresponding to a system with $L = 4$, for $\chi N = 10.4$,10.5 and 10.6. The density plots have been rescaled so that the difference in composition is clear. Light regions represents a majority of A-type segments, while dark regions correspond to a majority of B-type segments.

used for selecting the contour step Δs was such that the relative error in the reduced densities was less than 10^{-3}.

IV. Results and Discussion

A. The (Quasi) Mean-Field Regime. It is well-known that the ODT in the bulk occurs within mean-field theory for a symmetric diblock copolymer melt at $\chi N^* = 10.495$.[31] This holds true for a confined system with neutral walls, provided that the lamellae orient perpendicular to the walls (lamellae normal in the $x-y$ plane). The perpendicular orientation is to be expected because a parallel orientation would be energetically unfavorable when the width of the slit L is incommensurate with the equilibrium lamellar period D_l, resulting in stretching or compression of the layers. In the case of neutral surfaces, mean-field theory predicts that when the width L corresponds exactly to an integer multiple of $D_l/2$, both orientations are equally probable.[19,41]

We have studied the mean-field regime by setting the parameter $C \approx 20000$, which corresponds to unphysically large polymers ($N \sim 10^9$). To corroborate that we are in fact working in the mean field regime, we studied the ODT transition, and found that it occurs very near $\chi N = 10.5$, which is extremely close to the predicted mean-field result $\chi N^* = 10.495$ (data not shown). Although we are working in a "quasi'' mean-field regime, the Langevin simulations include fluctuations that lead to very small composition variations across the sample, from which we can extract information about the underlying density−density correlations. In Figure 1, we present snapshots of the

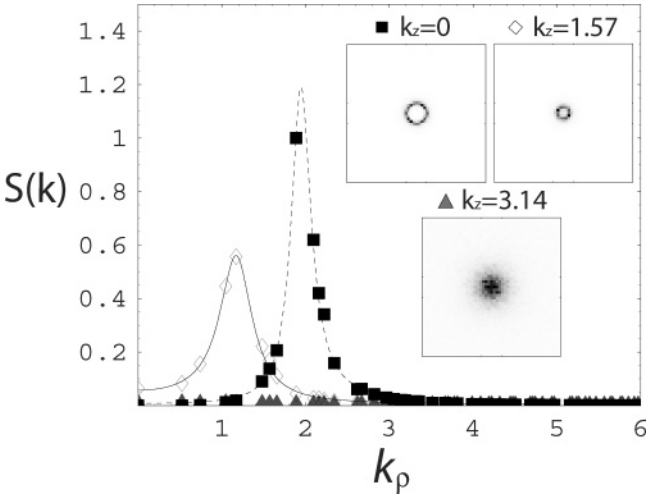

Figure 2. Structure factor $S(\mathbf{k})$ for a film with thickness $L = 2$ and $C \approx 20000$ at $\chi N = 10.4$. The values have been rescaled by the maximum value in the scattering data. The different symbols correspond to three different values of k_z:$k_z = 0$ (black squares), $k_z = 1.57$ (open diamonds), and $k_z = 3.14$ (gray triangles). The lines are two-parameter fits using eq 30 with the following parameters: $k_z = 0$, $\chi N = 10.421 \pm 0.003$, and $A = 0.000795 \pm 0.00001$ (dashed line), and $k_z = 1.57$, $\chi N = 10.421 \pm 0.002$, and $A = 0.00037 \pm 0.00001$ (solid line). Inset: the 2d scattering patterns for the different k_z values used in the graph. The plots have been rescaled so that the pattern is visible. The thin circle in the scattering data for $k_z = 0$ denotes the ring at which the Leibler structure factor has its maximum, and corresponds to a value of $k_\rho = 1.94$.

composition difference ϕ_- field for five different layers across the film of thickness $L = 4$ at $\chi N = 10.4$, 10.5, and 10.6. The density plots have been rescaled so that the difference in composition can be observed clearly. For reference, the lamellar equilibrium period is $D_l \approx 3.2$. It is interesting to note that at $\chi N = 10.5$ the different layers exhibit phase separation at different in-plane wave lengths. This can be seen directly from the figure, where it is obvious that the size of the domains being formed in the middle, and outer layers is larger than in the other two intermediate layers. We also note that when completely formed, the lamellae are not parallel to either axis in the $x-y$ plane, which is due to the incommensurability of the lamellar period with the lateral size ($12R_{go}$) of the box.

We further study the correlations in the sample by calculating the structure factor, as discussed in section IIB. In particular, we study two different film thicknesses, $L = 2$ and $L = 4$. In Figure 2, we show the circularly averaged structure factor for a film with thickness $L = 2$ at $\chi N = 10.4$. The lines correspond to the analytical structure factor derived by Leibler[31] for a symmetric diblock copolymer melt, given by

$$S(\mathbf{k}) = A\frac{\chi N(k_\rho^2 + k_z^2)^2}{\chi N(3 + e^{-(k_\rho^2+k_z^2)} - 4e^{-0.5(k_\rho^2+k_z^2)} - (k_\rho^2 + k_z^2)) + (k_\rho^2 + k_z^2)^2} \quad (30)$$

where $k_\rho^2 = k_x^2 + k_y^2$, and A is an amplitude that we have adjusted to fit the data. As is evident from the graph, the function $S(\mathbf{k})$ accurately fits the scattering data within the mean-field regime, except for the fact that the χN determined from the fit deviates slightly from its value in the simulation. Apart from this small deviation, we found that the amplitudes (contained within the figure caption) also vary depending on the value of the k_z mode.

Intuitively, one would expect the zero mode (along z) to dominate in an ultraconfined film, as the one under consideration, because it resembles a 2d system and distortions from

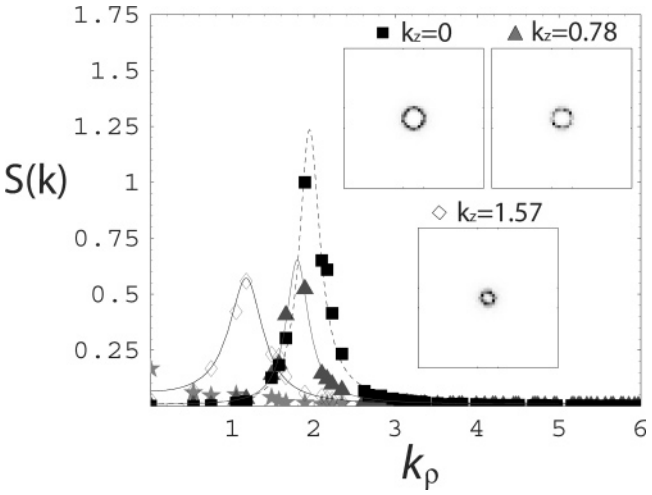

Figure 3. Structure factor $S(\mathbf{k})$ for a film with thickness $L = 4$ and $C \approx 20000$ at $\chi N = 10.4$. The values have been rescaled by the maximum value in the scattering data. The different symbols correspond to three different values of k_z:$k_z = 0$ (black squares), $k_z = 0.785$ (open diamonds), $k_z = 1.57$ (gray triangles), and $k_z = 2.355$ (gray stars). The lines are fits using eq 30 with the following parameters: $k_z = 0$, $\chi N = 10.41 \pm 0.01$, and $A = 0.00095 \pm 0.00005$ (dashed line), $k_z = 0.785$, $\chi N = 10.41 \pm 0.01$, and $A = 0.0005 \pm 0.00002$ (gray line), and $k_z = 1.57$, $\chi N = 10.41 \pm 0.01$, and $A = 0.00044 \pm 0.00004$ (solid line). Inset: the 2d scattering patterns for the different k_z values used in the graph. The plots have been rescaled so that the pattern is visible. The thin circle in the scattering data for $k_z = 0$ denotes the ring at which the Leibler structure factor has its maximum, and corresponds to a value of $k_\rho = 1.94$.

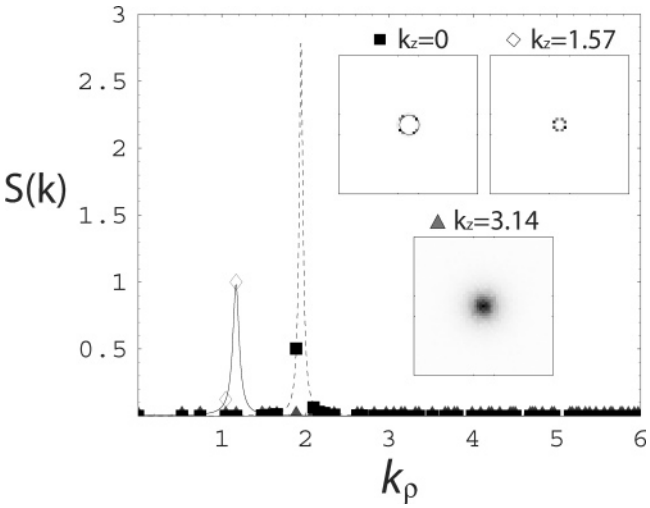

Figure 4. Structure factor $S(\mathbf{k})$ for a film with thickness $L = 2$ and $C \approx 20000$ at $\chi N = 10.5$. The values have been rescaled by the maximum value in the scattering data. The different symbols correspond to three different values of k_z:$k_z = 0$ (black squares), $k_z = 1.57$ (open diamonds), and $k_z = 3.14$ (gray triangles). The lines are fits using eq 30 with the following parameters: $k_z = 0$, $\chi N = 10.492 \pm 0.002$, and $A = 0.000067 \pm 0.000002$ (dashed line), and $k_z = 1.57$, $\chi N = 10.492 \pm 0.002$, and $A = 0.000024 \pm 0.000001$ (solid line). Inset: the 2d scattering patterns for the different k_z values used in the graph. The plots have been rescaled so that the pattern is visible. The thin circle in the scattering data for $k_z = 0$ denotes the ring at which the Leibler structure factor has its maximum, and corresponds to a value of $k_\rho = 1.94$.

uniformity along z are energetically costly. However, it can also be seen that the smallest nonzero $k_z = 1.57$ mode also contributes to the scattering pattern in a significant way. The increased importance of higher k_z modes is evident from Figure 3, where we have doubled the film thickness. Here, we observe that the $k_z = 0.78$, and the $k_z = 1.57$ modes are significantly populated. There is a marked difference with the bulk system in the sense that the maximum of the scattering peaks is not constant, but on the other hand, the system is driven to retain a spherical bulk-like structure factor, where the maximum scattering intensity occurs at $|\mathbf{k}| = 1.94$. The higher k_z modes do not contribute significantly because they are large compared to this value and are damped by interfacial energetics and conformational entropy.

The structure observed in the disordered confined film persists even at the onset of the ODT as shown in Figures 4 and 5, where we show the scattering data for $L = 2$ and $L = 4$ in the case of $\chi N = 10.5$. As can be seen from these plots, the only difference with the case of $\chi N = 10.4$ is that the peaks become considerably narrower, and the amplitude ratio between the higher modes and the zero mode becomes smaller. This is expected because the system will form perpendicular lamellae, which only contains the $k_z = 0$ mode. Nevertheless, the fact that the nonzero k_z modes are still present close to the transition is important since they may influence the melting of the structure under conditions of stronger fluctuations (i.e., at smaller C values). We also note that the χN obtained from the fit is $\chi N_{\text{fit}} = 10.492 \pm 0.002$, which corroborates that the simulations done at these parameters are mean-field simulations because the transition point is extremely close to $\chi N = 10.5$. Apart from this, the behavior exhibited in the quasi mean-field regime studied in this section serves as a guide to understand systems where fluctuations become much more significant, as will be the case in the next section.

B. Fluctuation Effects in Thin Polymer Films. We now turn to consider more realistic situations of confined block copolymer melts that exhibit significant fluctuations in composition near the ODT. In this section we tackle the case of $C = 50$, which corresponds to a typical polymerization index of $N \sim 10^5$.

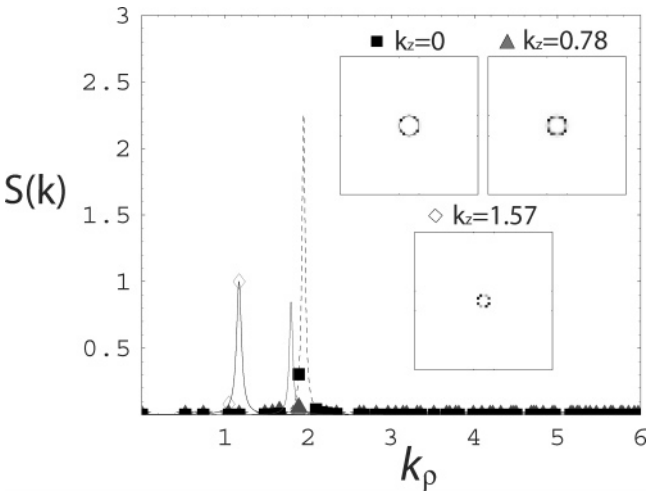

Figure 5. Structure factor $S(\mathbf{k})$ for a film with thickness $L = 4$ and $C \approx 20000$ at $\chi N = 10.5$. The values have been rescaled by the maximum value in the scattering data. The different symbols correspond to three different values of k_z:$k_z = 0$ (black squares), $k_z = 0.785$ (open diamonds), $k_z = 1.57$ (gray triangles), and $k_z = 2.355$ (gray stars). The lines are fits using eq 30 with the following parameters: $k_z = 0$, $\chi N = 10.493 \pm 0.0002$, and $A = 0.0000389 \pm 0.0000003$ (dashed line), $k_z = 0.785$, $\chi N = 10.493 \pm 0.0002$, and $A = 0.0000145 \pm 0.0000004$ (gray line), and $k_z = 1.57$, $\chi N = 10.493 \pm 0.0002$, and $A = 0.0000147 \pm 0.0000003$ (solid line). Inset: the 2d scattering patterns for the different k_z values used in the graph. The plots have been rescaled so that the pattern is visible. The thin circle in the scattering data for $k_z = 0$ denotes the ring at which the Leibler structure factor has its maximum, and corresponds to a value of $k_\rho = 1.94$.

In Figure 6, we present snapshots of the some of the different films studied in this section. The upper row corresponds to

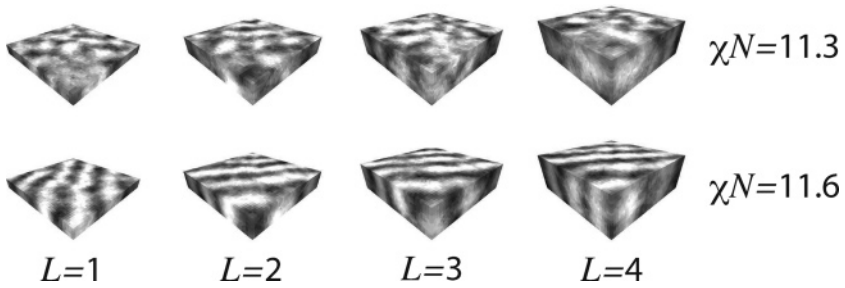

Figure 6. Snapshots of the instantaneous ϕ_- field for different film thicknesses L in the disordered (upper row) and the ordered (lower row) phases.

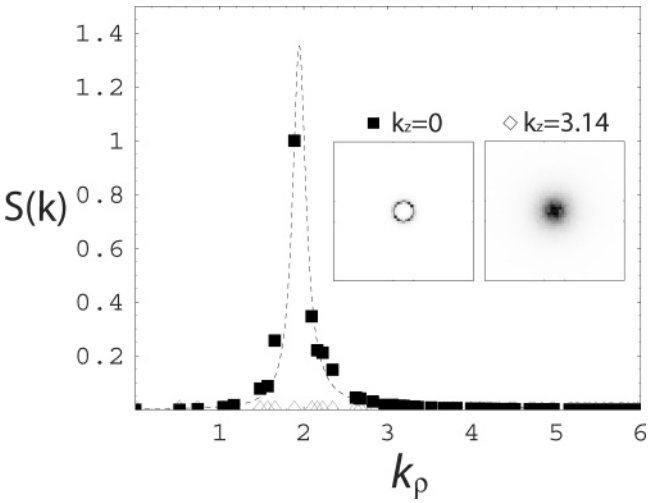

Figure 7. Structure factor $S(\mathbf{k})$ for a film with thickness $L = 1$ and $C = 50$ at $\chi N = 11.3$. The values have been rescaled by the maximum value in the scattering data. The different symbols correspond to three different values of k_z:$k_z = 0$ (black squares), $k_z = 3.14$ (open diamonds). The line is a fit using eq 30 with the following parameters: $k_z = 0$, $\chi N = 10.461 \pm 0.006$, and $A = 0.00041 \pm 0.00005$ (dashed line). Inset: the 2d scattering patterns for the different k_z values used in the graph. The plots have been rescaled so that the pattern is visible. The thin circle in the scattering data for $k_z = 0$ denotes the ring at which the Leibler structure factor has its maximum, and corresponds to a value of $k_\rho = 1.94$.

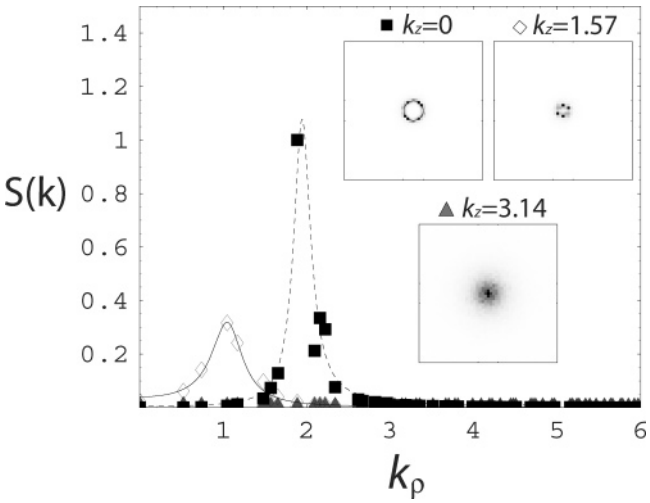

Figure 8. Structure factor $S(\mathbf{k})$ for a film with thickness $L = 2$ and $C = 50$ at $\chi N = 11.4$. The values have been rescaled by the maximum value in the scattering data. The different symbols correspond to three different values of k_z:$k_z = 0$ (black squares), $k_z = 1.57$ (open diamonds), $k_z = 3.14$ (gray triangles). The lines are fits using eq 30 with the following parameters: $k_z = 0$, $\chi N = 10.46 \pm 0.007$, and $A = 0.00054 \pm 0.00006$ (dashed line), and $k_z = 1.64 \pm 0.02$, $\chi N = 10.46 \pm 0.007$, and $A = 0.00016 \pm 0.00002$ (solid line). Inset: the 2d scattering patterns for the different k_z values used in the graph. The plots have been rescaled so that the pattern is visible. The thin circle in the scattering data for $k_z = 0$ denotes the ring at which the Leibler structure factor has its maximum, and corresponds to a value of $k_\rho = 1.94$.

disordered states, while the lower row contains ordered configurations obtained at larger χN values. It is important to note from the snapshots that the ordered configurations still display pronounced fluctuations seen as undulations of the lamellae, or topological defects in the layers. Nevertheless, they possess a broken symmetry consistent with a perpendicular lamellar phase that is manifest in the structure factor as will be shown later.

The Disordered Phase. As in the previous section, we will start by describing the disordered state of this system with $C = 50$ for different film thicknesses. In particular, we concentrate on $L = 1$ and $L = 2$ because they exemplify what occurs for thin films. Likewise, we will use the structure factor $S(\mathbf{k})$ to extract useful information about the underlying correlations in the samples.

In Figure 7, we present the scattering pattern for a film of thickness $L = 1$. As can be seen from the plot, the strongest mode in this case corresponds to $k_z = 0$, while the higher modes are essentially negligible. This is because all other modes have wave vectors significantly higher than the Leibler shell value quoted above. It follows that the $k_z = 0$ mode is the only one populated in all copolymer films with thicknesses below $L = 1$. Such ultra-confined films resemble 2d systems, because composition variations are restricted to the $x-y$ plane. We also note that the Leibler scattering function fits the data quite well, making it possible to extract useful information about the location and height of the maximum of the structure factor by fitting χN and A. For this particular case, $L = 1$, and $\chi N = 10.4$ we find that the best fitting parameters are $A \approx 0.00041$, and $\chi N_{\text{fit}} \approx 10.46$, implying that one is close to the ODT. Nevertheless, as shown in the two-dimensional scattering patterns, the system is still isotropic in the $x-y$ plane.

The situation is quite different for thicker films when one allows the nonzero k_z modes to become relevant, as shown in Figure 8 for a film with $L = 2$. As seen in the figure the scattering intensity of the $k_z = 1.57$ mode is not negligible in this case. The data is still well-fit by eq 18. Also, we note that the k_z obtained from the fit for the nonzero mode does not correspond to the pure harmonic value $k_z = 1.57$, but it is rather $k_z^{\text{fit}} \approx 1.64$. This implies that the spherical structure factor has become distorted, and resembles an ellipsoid of revolution, with its larger axis in the $x-y$ plane.

The Onset of the Order—Disorder Transition and the Ordered Phase. From our previous findings, we expect that the confinement effects observed before will be accentuated at larger χN values close to the ODT. In Figures 9−12, we present scattering data for films with thicknesses $L = 1, 2, 3, 4$. In general, we note that, apart from the case $L = 1$, all the other films scatter significantly at nonzero k_z modes, particularly the thicker films. Also, we note that the two-dimensional patterns

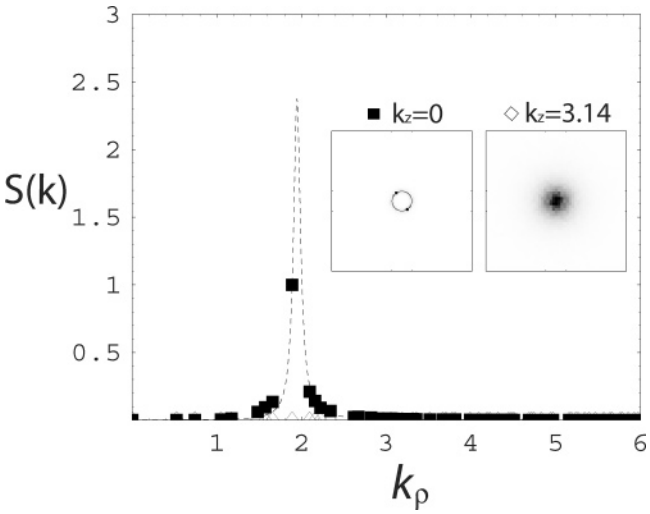

Figure 9. Structure factor $S(\mathbf{k})$ for a film with thickness $L = 1$ and $C = 50$ at $\chi N = 11.4$. The values have been rescaled by the maximum value in the scattering data. The different symbols correspond to three different values of k_z:$k_z = 0$ (black squares), $k_z = 3.14$ (open diamonds). The line is a fit using eq 30 with the following parameters: $k_z = 0$, $\chi N = 10.485 \pm 0.003$, and $A = 0.00019 \pm 0.00002$ (dashed line). Inset: the 2d scattering patterns for the different k_z values used in the graph. The plots have been rescaled so that the pattern is visible. The thin circle in the scattering data for $k_z = 0$ denotes the ring at which the Leibler structure factor has its maximum, and corresponds to a value of $k_\rho = 1.94$.

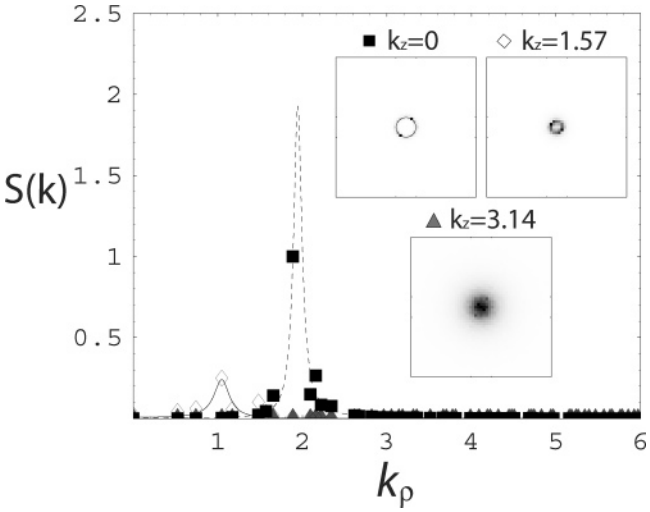

Figure 10. Structure factor $S(\mathbf{k})$ for a film with thickness $L = 2$ and $C = 50$ at $\chi N = 11.5$. The values have been rescaled by the maximum value in the scattering data. The different symbols correspond to three different values of k_z:$k_z = 0$ (black squares), $k_z = 1.57$ (open diamonds), $k_z = 3.14$ (gray triangles). The lines are fits using eq 30 with the following parameters: $k_z = 0$, $\chi N = 10.482 \pm 0.001$, and $A = 0.000225 \pm 0.00004$ (dashed line), and $k_z = 1.64 \pm 0.02$, $\chi N = 10.482 \pm 0.001$, and $A = 0.000028$ (solid line). Inset: the 2d scattering patterns for the different k_z values used in the graph. The plots have been rescaled so that the pattern is visible. The thin circle in the scattering data for $k_z = 0$ denotes the ring at which the Leibler structure factor has its maximum, and corresponds to a value of $k_\rho = 1.94$.

become quite anisotropic, but nevertheless the structures are still disordered (as will be shown later). It is interesting also to observe that the shifts in the values of the fitted k_z's remain. However, the "sign'' of the shift becomes thickness dependent. To see this clearly, we compare the shifts from the films with $L = 3$ and $L = 4$. In the case $L = 3$, we note that the fitted value for the $k_z = 1.05$ mode results in $k_z^{\text{fit}} = 0.837$. This implies that the structure factor in this case would become somewhat steeper along the k_z axis. Interestingly, for the case

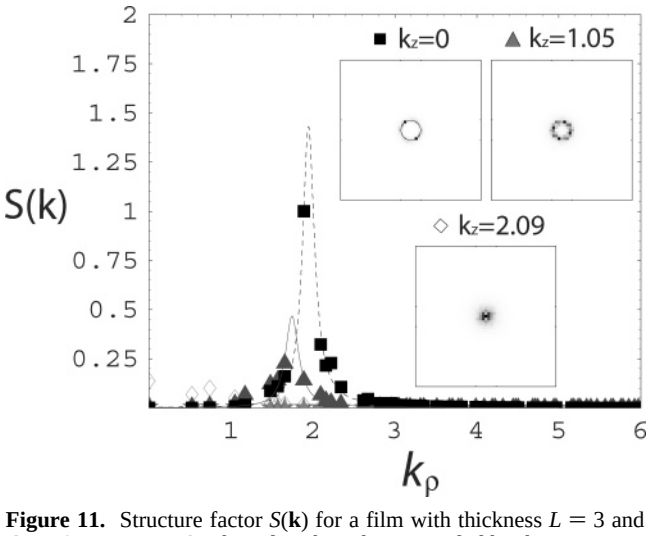

Figure 11. Structure factor $S(\mathbf{k})$ for a film with thickness $L = 3$ and $C = 50$ at $\chi N = 11.3$. The values have been rescaled by the maximum value in the scattering data. The different symbols correspond to three different values of k_z:$k_z = 0$ (black squares), $k_z = 1.047$ (gray triangles), and $k_z = 2.094$ (open diamonds). The lines are fits using eq 30 with the following parameters: $k_z = 0$, $\chi N = 10.488 \pm 0.002$, and $A = 0.00017 \pm 0.00002$ (dashed line), and $k_z = 0.83 \pm 0.01$, $\chi N = 10.488 \pm 0.002$, and $A = 0.000072 \pm 0.000005$ (gray line). Inset: the 2d scattering patterns for the different k_z values used in the graph. The plot have been rescaled so that the pattern is visible. The thin circle in the scattering data for $k_z = 0$ denotes the ring at which the Leibler structure factor has its maximum, and corresponds to a value of $k_\rho = 1.94$.

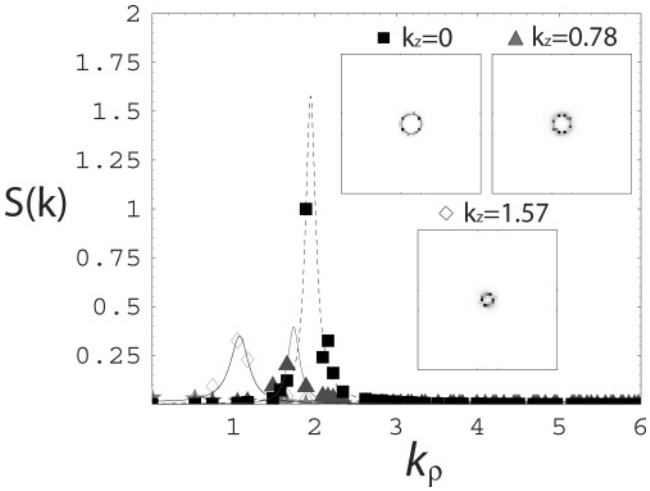

Figure 12. Structure factor $S(\mathbf{k})$ for a film with thickness $L = 4$ and $C = 50$ at $\chi N = 11.3$. The values have been rescaled by the maximum value in the scattering data. The different symbols correspond to three different values of k_z:$k_z = 0$ (black squares), $k_z = 0.785$ (open diamonds), $k_z = 1.57$ (gray triangles), and $k_z = 2.355$ (gray stars). The lines are fits using eq 30 with the following parameters: $k_z = 0$, $\chi N = 10.47 \pm 0.004$, and $A = 0.0003 \pm 0.00004$ (dashed line), $k_z = 0.87 \pm 0.01$, $\chi N = 10.47 \pm 0.004$, and $A = 0.000075 \pm 0.000003$ (gray line), and $k_z = 1.62 \pm 0.01$, $\chi N = 10.47 \pm 0.004$, and $A = 0.000066 \pm 0.000003$ (solid line). Inset: the 2d scattering patterns for the different k_z values used in the graph. The plot have been rescaled so that the pattern is visible. The thin circle in the scattering data for $k_z = 0$ denotes the ring at which the Leibler structure factor has its maximum and corresponds to a value of $k_\rho = 1.94$.

$L = 4$ (and similarly for $L = 2$), the fitted value for the $k_z = 1.57$ is $k_z^{\text{fit}} = 1.62$, which implies that the structure factor becomes somewhat flatter. It is also important to note that the fits to the Leibler structure factor are not as accurate as in the mean-field case of $C = 20\,000$. Nevertheless they are useful for extracting qualitative trends from our simulations.

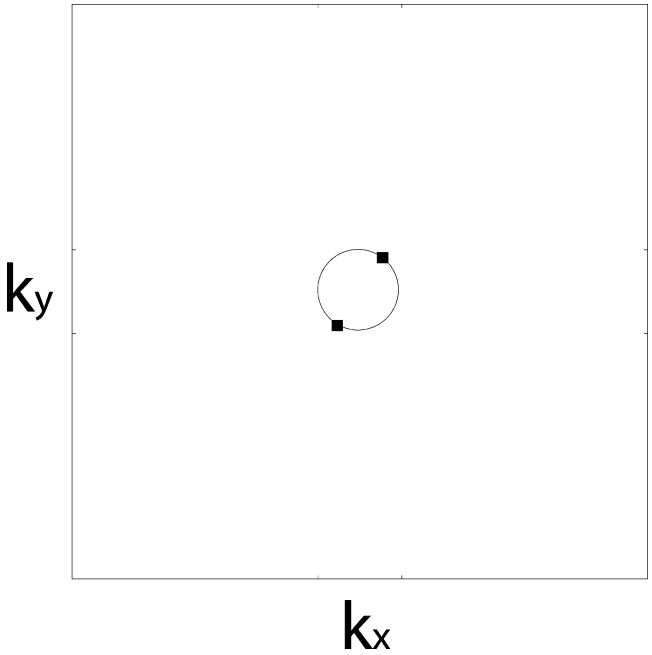

Figure 13. Typical structure factor ($k_z = 0$ mode) of the ordered phase from a simulation with $L = 4$ and $\chi N = 11.5$. The circle corresponds to the location of the predicted maximum of the structure factor in the disordered phase.

Finally, we present in Figure 13 the two-dimensional structure factor for the lamellar state. This structure factor corresponds to the $k_z = 0$ mode, and for a film with $L = 4$, and $\chi N = 11.5$. All other k_z modes become negligible at this value of χN. As expected, it consist of two peaks, located (within the resolution of our grid) at the predicted microdomain length scale $k_z = 1.89$. The peaks are oriented at an angle, and this is due to the fact that the lateral box dimensions do not correspond to an integer multiple of lamellae, which forces the lamellae to orient at an oblique angle.

The ODT under Confinement. It is now of interest to explore whether the film thickness and the fluctuation phenomena that we just presented have a role in the location of the ODT. To locate the ODT, we used the order parameter Ψ introduced in section IIB. All the simulation results presented in this section were obtained by starting in an ordered configuration, and slowly reducing the χN parameter until a disordered state was achieved. This is analogous to heating a real block copolymer film across the order−disorder boundary. From prior experience, we have found that the ODT hysteresis is smaller on superheating as opposed to supercooling.[36] In Figure 14, we present the results for the value of the order parameter Ψ over a range of χN values and different film thicknesses L. An important feature of this graph is that Ψ exhibits a pronounced jump in its value across the ODT. This behavior had been observed before in the work of Vasiliev and Matsen.[30] Other ways of characterizing the ODT have been described in the work by Duechs et al.,[47] but we found the discontinuous change in Ψ to be the most straightforward way to locate the ODT. The transition is taken to occur at the midpoint of the steepest decrease in Ψ upon lowering χN. For example, in the case of $L = 0.5$, we see that the value of Ψ decreases most abruptly between $\chi N = 11.8$ and $\chi N = 11.7$, so we locate the ODT at $\chi N = 11.75 \pm 0.05$.

A phase diagram constructed from simulation data for all the film thicknesses studied in this work is presented in Figure 15. From the figure it can be seen that the ODT is strongly suppressed for ultrathin films of thickness $L < 1$, but for $L \geq 1$

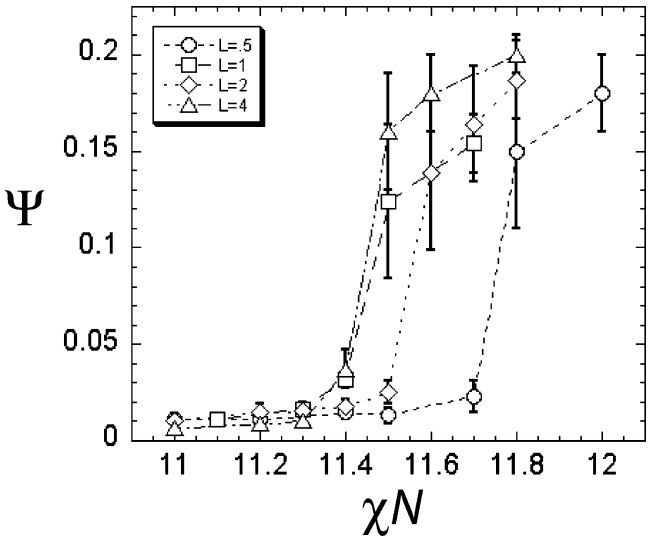

Figure 14. Order parameter Ψ defined in eq 19.

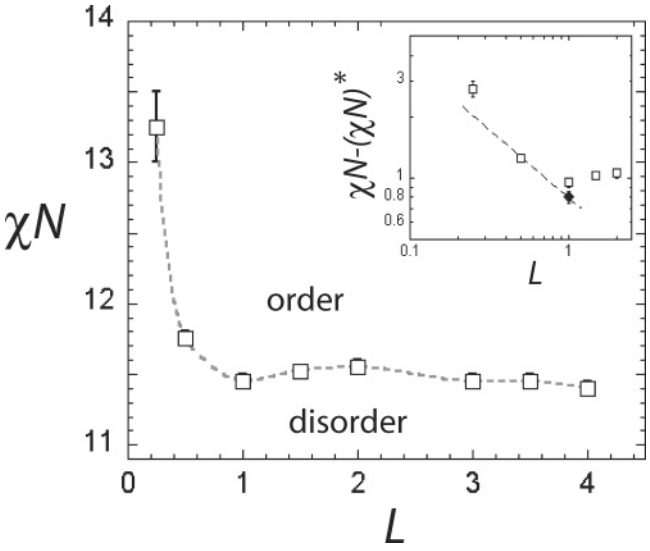

Figure 15. Phase diagram for a confined symmetric diblock copolymer. Inset: the phase diagram plotted in a log−log scale as a function of the new variable $\chi N - \chi N^*$, where $\chi N^* = 10.5$. The line is the Fredrickson−Helfand prediction for the shift in the ODT (see text for details), and the black diamond is the simulation result for a pure 2d system, taken from refs 36, 47, and 56.

it is relatively insensitive to L, except for a weak maximum at $L \approx 2$. In this case, the ODT occurs at $\chi N = 11.55 \pm 0.05$, which corresponds to approximately a 10 % shift in the ODT with respect to the mean-field value of $\chi N^* = 10.495$.

Our results are in qualitative agreement with the recent the analytical treatment of Shi and co-workers.[27] Nevertheless, there are some discrepancies. For example, we find the minimum width at which there is a strong increase in the ODT to be $L \sim 1R_{go}$ compared to the value they quote of $\sim 1.5R_{go}$. This difference might be due to the approximations involved in the analytical treatment. Also, the weak maximum in the ODT temperature we observe near $L = 2$ is missing from their results. Although we do not fully understand the mechanism that produces this feature, there seems to be a competition between a tendency of the ends to be near (attracted to) the surface, and thus frustrate the ordering, and the segmental interactions driving the microphase separation. For thick films, the segmental interactions dominate since they scale with the volume of the confined region, while for very thin films the composition

correlation length is larger than the film thickness, which renders the system effectively 2-dimensional and produces a large positive shift in the ODT (as discussed further below). Only for intermediate film thicknesses, e.g., $L = 2$, can chain end effects likely be seen, and we believe this is the origin of the non-monotonic dependence of the transition temperature on L.

The behavior observed for the thinnest films can be viewed as a type of confinement induced melting. Notice that this mechanism does not invoke any preferential wetting conditions, since all the simulations conducted here involved neutral walls. Similar behavior was recently found in a triblock system using particle-based simulations.[43] Experimentally, we believe that this mechanism will become relevant for ultrathin films confined by neutral surfaces, and may be the cause of the observed melting of triblock copolymers thin films at thicknesses small compared to the period of the microphase structure.[54,55] An explanation for this behavior can be constructed as follows. Consider that the $k_z = 0$ mode is the only non-negligible mode, which is a reasonable assumption based on the results shown previously for $L = 1$. In this case, we can think of a 3d film with $L < 1$ as a 2d film, in which the L-dependent parameter $C(L) = L \cdot C$ replaces the 3d Ginzburg parameter C. According to the asymptotic analysis of Fredrickson and Helfand,[32] and confirmed in 2d simulations by Ganesan and Fredrickson,[36] this would induce a shift compared to χN^* in the ODT proportional to $C(L)^{-2/3} \sim L^{-2/3}$. Another way of rationalizing this result is by noting that $\Delta\chi \sim C^{-2/3}$ in 2d and 3d, where C is as before given by $C = \rho_0 R_{go}{}^d/N$. A simple extrapolation for the average total density from 2d ($L \rightarrow 0$) to 3d ($L \rightarrow \infty$) can be constructed as

$$C(L) \sim \frac{\rho_0 R_{go}{}^3}{N} f(L/R_{go}) \tag{31}$$

with

$$f(x) = \begin{cases} x & \text{if } x \ll 1, \\ 1 & \text{if } x \gg 1 \end{cases} \tag{32}$$

We note that L in this case has dimensions of length. Notice that this result also explains the saturation at large L and that in the limit $C \rightarrow \infty$ one will always recover the self-consistent mean field transition temperature no matter how thin the polymer layer is. In the inset of Figure 15, we show a graph of the shift from the mean-field ODT plotted on a log−log scale. The dashed line has a slope of −2/3. The black diamond corresponds to the pure 2d result for a concentration of $C = 50$, and it was taken from previously published studies.[36,47,56] As can be seen, the data follows the line for the larger values of $L \leq 1$, but it deviates from the data point for the smallest value of L. This can likely be attributed to the fact that in this regime the asymptotic analytical theory is no longer valid because the value of $C(L)$ is too small.

V. Conclusions

In summary, we have presented field-theoretic simulation data for thin films of diblock copolymer melts. Our work was performed under the condition of neutral walls separated by a distance L, but can be extended to include preferential wetting effects by applying appropriate boundary conditions at the surfaces of the film.[35] Overall, we found that confinement significantly influences the spectrum of composition fluctuations in symmetric diblock copolymer melts, although for thicknesses $L3$ (units of R_{go}) the spectrum retains most of the features of a bulk system. For large values of the Ginzburg parameter C, or equivalently chain length N, the structure−function has its maximum at the predicted values from the RPA theory, although the height of the maximum varies among the different k_z longitudinal modes. The location of the peaks is well described by the RPA theory in this quasi-mean-field regime. In contrast, with the inclusion of stronger fluctuations, i.e., smaller values of C, we observed a shift in the location of the nonzero longitudinal mode peaks. This shift was shown to be film thickness dependent.

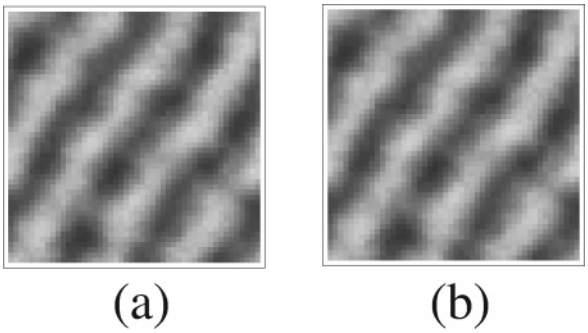

Figure 16. Snapshots of the instantaneous composition difference $\phi_-(\mathbf{r})$ for a fixed Ω_- field corresponding to $\chi N = 11.45$. The density plot labeled (a) is the original configuration calculated using the saddle-point approximation, and (b) corresponds to an instantaneous configuration along the complex Langevin sampling. The density plots have been rescaled so that the difference in composition is clear. Light regions represents a majority of A-type monomer, while dark regions correspond to a majority of B-type monomer.

Apart from the analysis of confinement on composition fluctuations, we also studied the location of the ODT as a function of film thickness. A confinement-induced melting transition was observed for ultrathin films characterized by $L < 1$, while the location of the ODT remained fairly constant for the larger film thicknesses studied. Although we do not have experimental evidence in support of all the findings presented here, we believe that these results could be confirmed by X-ray scattering experiments on thin films that resolve the k_z and k_ρ modes separately.[45]

It would be desirable to extend the present studies to thin films of asymmetric block copolymers, to other block copolymer architectures, and to block copolymer solutions and alloys, where confinement might induce more dramatic and potentially useful changes in ordering behavior.

Appendix

A. Validity of the Saddle-Point Approximation. In this appendix we consider the validity of evaluating $Z[\Omega_-]$ by the partial saddle-point approximation. Specifically, we present numerical evidence that this approximation is reasonably accurate for the parameters used in our simulations. We test this assumption by considering a typical, but fixed, Ω_- configuration that corresponds to a quasi-ordered structure (shown in Figure 16) and examine the validity of the neglect of Ω_+ fluctuations in the partial saddle point approximation by direct integration of $Z[\Omega_-]$ using a complex Langevin (CL) scheme described in a previous publication.[57]

As can be seen from eq 20, we can calculate the full partition function by integrating first over the Ω_+ field to obtain $Z[\Omega_-]$, and then integrating over the Ω_- field. In order to apply this scheme, we need to evaluate $Z[\Omega_-]$ for every different configuration of the Ω_- field. Applying a Langevin algorithm for the evolution of the minus field implies that we write the partition

function as

$$Z \propto \int \mathcal{D}\Omega_- \, e^{-H[\Omega_-]} \tag{A1}$$

where the Hamiltonian $H[\Omega_-]$ is given by

$$H[\Omega_-] = -\ln(Z[\Omega_-]) + \frac{C}{\chi N}\int \mathrm{dr}\,[\Omega_-(\mathbf{r})]^2 \tag{A2}$$

The dissipative term of the Langevin equation, $-\delta H[\Omega_-]/\delta\Omega_-$, is calculated as

$$\begin{aligned} -\frac{\delta H[\Omega_-]}{\delta\Omega_-} &= \frac{\delta(\ln(Z[\Omega_-]))}{\delta\Omega_-} - \frac{2C}{\chi N}\Omega_-(\mathbf{r}) \\ &= \frac{1}{Z[\Omega_-]}\frac{\delta Z[\Omega_-]}{\delta\Omega_-} - \frac{2C}{\chi N}\Omega_-(\mathbf{r}) \\ &= C\left(\langle\phi_-(\mathbf{r};[\Omega_-])\rangle_{\Omega+} - \frac{2}{\chi N}\Omega_-(\mathbf{r})\right), \end{aligned} \tag{A3}$$

where $\langle\cdots\rangle_{\Omega_+}$ denotes an average taken over the Ω_+ configurations.

To quantify the error involved in using the partial saddle-point approximation (PSPA), we calculate the mean and variance of the following quantity

$$\Delta\phi_- = \langle\phi_-(\mathbf{r};[\Omega_-])\rangle_{\Omega_+} - \phi_-(\mathrm{r};[\Omega_+^*,\Omega_-]) \tag{A4}$$

which corresponds to the difference between the average composition difference generated by the full complex Langevin integration, compared to that generated by the PSPA. It is important to evaluate $\Delta\phi_-$ since it will contribute to the update of the Ω_- field, and if it is small in magnitude (i.e., $|\Delta\phi| \ll 1$), we can assume that the partial saddle-point approximation is accurate enough to approximate the partition function $Z[\Omega_-]$.

We have performed the CL simulation for this test on a 48 $\times$ 48 square lattice of side length 12 (in units of R_{go}), and lattice discretization dx = dy = 0.25. Periodic boundary conditions are applied in both directions. The value of the concentration is set to $C = 50$, and the fixed Ω_- field corresponds to a configuration that has been selected from a simulation run equilibrated at $\chi N = 11.45$. For reference, the order−disorder transition (ODT) occurs for this system at $\chi N^* \sim 11.35$, which implies we are still within the window of large fluctuations due to the closeness to the transition temperature.

In Figure 17, we present a histogram of $\Delta\phi_-$ collected from the CL simulation average of $\phi_-(\mathbf{r};[\Omega_-])$ across the 48^2 sites of the lattice. The mean $\Delta\bar{\phi}_-$ and the variance $\sigma_{\phi-}{}^2$ for this distribution are calculated to be $\Delta\bar{\phi}_- = -1.7 \times 10^{-7}$ and $\sigma_{\phi-}{}^2 = 3.1 \times 10^{-5}$, which are extremely small and would lead to negligible changes in the dynamics as long as $\Delta\phi_-$ is not correlated with the dissipation term. To show so, we display in Figure 18 a histogram of the sign-correlation function

$$c(\mathbf{r}) = \Delta\phi_-(\mathbf{r}) \times (\phi_-(\mathbf{r}) - (2/\chi N)\Omega_-(\mathbf{r})) \tag{A5}$$

The histogram labeled (a) corresponds to the values of $c(\mathbf{r})$ using $\phi_-(\mathbf{r}) = \phi_-(\mathbf{r};[\Omega_-,\Omega_+^*])$, while the histogram labeled (b) represents the values of $c(\mathbf{r})$ using $\phi_-(\mathbf{r}) = \langle\phi_-(\mathbf{r};[\Omega_-])\rangle_{\Omega+}$. As seen from this figure, there is no indication that there exist any correlation between the sign of $\Delta\phi_-(\mathbf{r})$ and the sign of the dissipation term. If there was a correlation in the sign, the distribution would be asymmetrical with respect to zero. At most, one can conclude that the high peak implies a correlation on the relative values of both of these quantities. In any case, we only need to know that the sign is not correlated in order to argue that the deviations will alter the dynamics only as an extra source of noise.

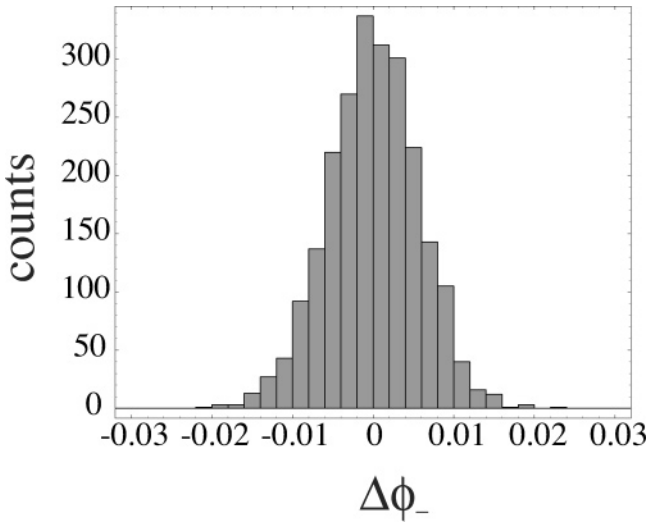

Figure 17. Histogram of $\Delta\phi_-$.

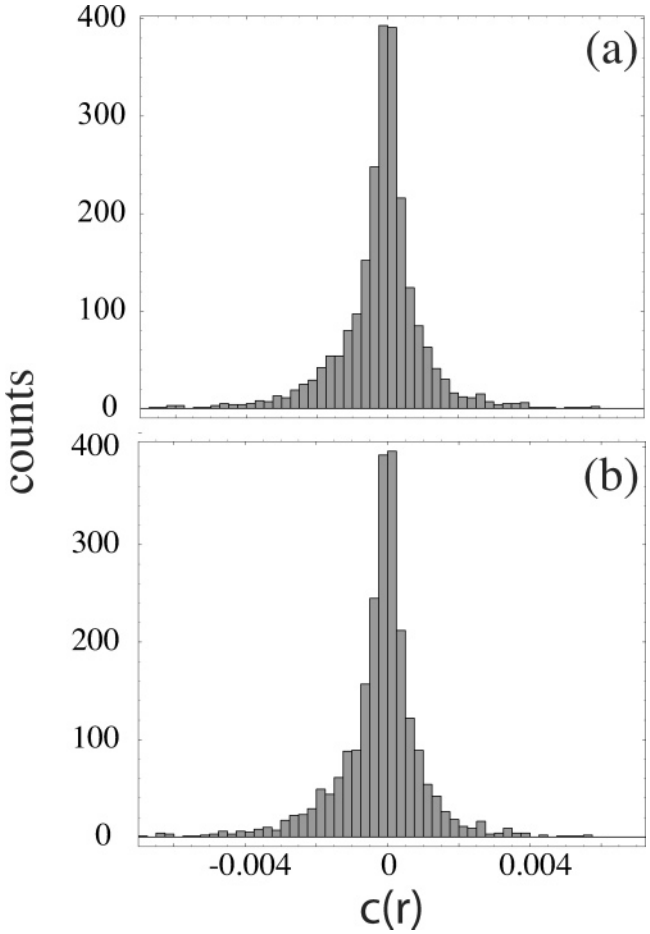

Figure 18. Histogram of the correlation function $c(\mathbf{r})$. The plot labeled (a) corresponds to the values of $c(\mathbf{r})$ using $\phi_-(\mathbf{r}) = \phi_-(\mathbf{r};[\Omega_-,\Omega_+^*])$, while the histogram labeled (b) represents the values of $c(\mathbf{r})$ using $\phi_-(\mathbf{r}) = \langle\phi_-(\mathbf{r};[\Omega_-])\rangle_{\Omega+}$.

A simple argument for the validity of the PSPA is as follows: consider the standard deviation $\sqrt{\sigma_{\phi-}{}^2}$ as the typical measure of the difference between the PSPA and the CL results for ϕ_-. For a given update of the field Ω_-, the typical value of the extra noise term would scale as $\Delta t\Delta^2 rC\sqrt{\sigma_{\phi-}{}^2}/2$. For the

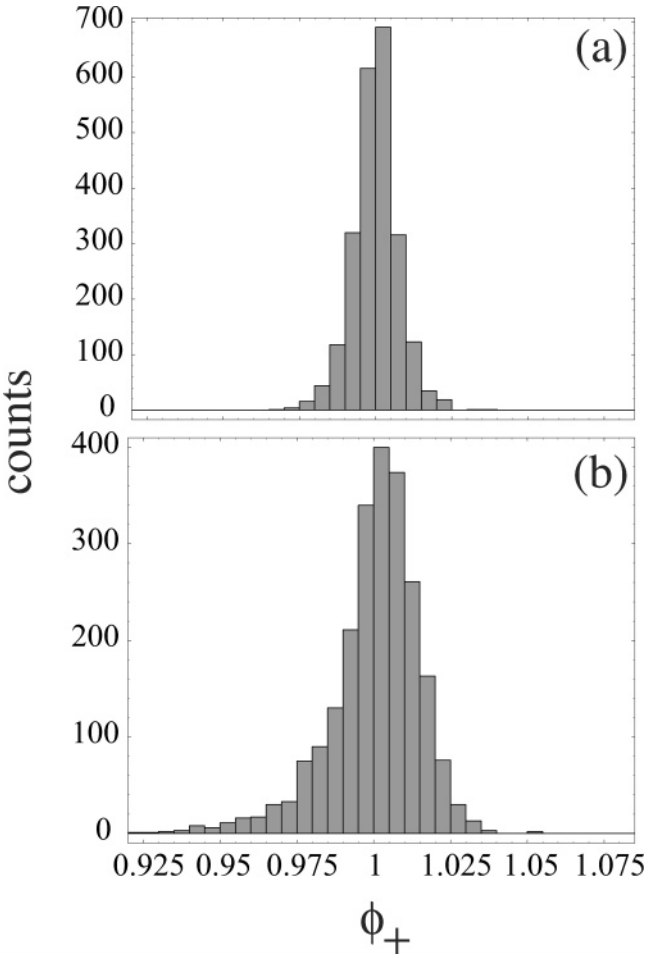

Figure 19. Histogram of the total reduced density $\phi_+(\mathbf{r})$ corresponding to (a) the SPA, and (b) along the CL trajectory.

parameters used in our simulation this quantity is approximately $\sim 9 \times 10^{-5}$, while the typical value of the actual noise term is $\sqrt{\Delta t} \sim 10^{-1}$. The ratio of these two quantities is of order $\sim 10^{-3}$, which implies that the PSPA should be very accurate, at least for the parameters employed in our simulations. This argument is corroborated by Figure 16, where the density plot labeled b corresponds to a snapshot of the ϕ_- density field along the CL trajectory, while part a represents the original ϕ_- density field calculated through the partial saddle point approximation. The prescribed accuracy in the dispersion of the total density used in the latter computations was $\sqrt{\sigma} < 0.0075$.

To finalize our discussion, we present in Figure 19 a comparison of the spatial distribution of the total reduced density $\phi_+(\mathbf{r})$. The histogram in part a corresponds to the original configuration of the density field, i.e., $\phi_+(r; [\Omega_-,\Omega_+^*])$, which was generated as described in the previous section, while part b corresponds to a histogram of a typical configuration along the complex Langevin trayectory $\phi_-(r; [\Omega_-,\Omega_+,])$. As can be seen from this figure, the dispersion of the total density is about twice as large using CL, as compared to the PSP approximation.

Acknowledgment. This work was supported in part by NSF CMMT Grant DMR06−03710. G.H.F. is also pleased to acknowledge support from MARCO FENA at UCLA. Extensive use was made of the MRL Central Computing Facility supported by the MRSEC Program of the NSF under award No. DMR05−20415. A.A.-K. is also grateful to the NSF for funding through an international postdoctoral fellowship.

References and Notes

(1) Bates, F. S.; Fredrickson, G. H. *Phys. Today* **1999**, *52*, 32.
(2) Hamley, I. W. *The Physics of Block Copolymers*; Oxford University Press: Oxford, U.K., 1998.
(3) Park, M.; Harrison, C.; Chaikin, P. M.; Register, R. A.; Adamson, D. H. *Science* **1997**, *276*, 1401.
(4) Cohen, R. D. *Curr. Opin. Solid State Mater. Sci.* **1999**, *4*, 587.
(5) Thurn-Albrecht, T.; Schotter, J.; Kaestle, G. A.; Emley, N.; Shibauchi, T.; Krusin-Elbaum, L.; Guarini, K.; Black, C. T.; Tuominen, M.; Russell, T. P. *Science* **2000**, *290*, 2126.
(6) Thurn-Albrecht, T.; Steiner, R.; DeRouchey, J.; Stafford, C. M.; Huang, E.; Bal, M.; Tuominen, M.; Hawker, C. J.; Russell, T. P. *Adv. Mater.* **2000**, *12*, 787.
(7) Bockstaller, M. R.; Mickiewicz, R. A.; Thomas, E. L. *Adv. Mater.* **2005**, *17*, 1331.
(8) Wu, T;, Cheng, G.; Katsov, K;, Sides, S. W.; Wang, J.; Tang, J.; Fredrickson, G. H.; Moskovits, M.; Stucky, G. D. *Nat. Mater.* **2004**, *3*, 816.
(9) Segalman, R. A.; Hexemer, A.; Hayward, R. C.; Kramer, E. J. *Macromolecules* **2003**, *36*, 3272.
(10) Segalman, R. A.; Hexemer, A.; Kramer, E. J. *Phys. Rev. Lett.* **2003**, *91*, 196101.
(11) Xu, T.; Goldbach, J. T.; Misner, M. J.; Kim, S.; Gibaud, A.; Gang, O.; Ocko, B.; Guarini, K. W.; Black, C. T.; Hawker, C. J.; Russel, T. P. *Macromolecules* **2004**, *37*, 2972.
(12) Angelescu, D. E.; Harrison, C. K.; Trawick, M. L.; Register, R. A.; Chaikin, P. M. *Phys. Rev. Lett.* **2005**, *95*, 025702.
(13) Green, P. F.; Limary, R. *Adv. Colloid Interface Sci.* **2001**, *94*, 53.
(14) Lambooy, P.; Russell, T. P.; Kellog, G. J.; Mayes, A. M.; Gallagher, P. D.; Satija, S. K. *Phys. Rev. Lett.* **1994**, *72*, 2899.
(15) Kellog, G. J.; Walton, D. G.; Mayes, A. M.; Lambooy, P.; Russell, T. P.; Gallagher, P. D.; Satija, S. K. *Phys. Rev. Lett.* **1996**, *76*, 2503.
(16) Sikka, M.; Singh, N.; Karim, A.; Bates, F. S.; Satija, S. K.; Majkrzak, C. F. *Phys. Rev. Lett.* **1993**, *70*, 307.
(17) Morkved, T. L.; Jaeger, H. J. *Europhys. Lett.* **1997**, *40*, 643.
(18) Menelle, A.; Rusell, T. P.; Anastasiadis, S. H.; Satija, S. K.; Majkrzak, C. F. *Phys. Rev. Lett.* **1992**, *68*, 67.
(19) Tsori, Y.; Andelman, D. *Eur. Phys. J. E* **2001**, *5*, 605.
(20) Milner, S. T.; Morse, D. C. *Phys. Rev. E* **1996**, *54*, 3793.
(21) Binder, K. *Adv. Polym. Sci.* **1999**, *138*, 1.
(22) Pickett, G. T.; Balazs, A. C. *Macromolecules* **1997**, *30*, 3097.
(23) Matsen, M. W. *J. Chem. Phys.* **1997**, *106*, 7781.
(24) Geisinger, T.; Mueller, M.; Binder, K. *J. Chem. Phys.* **1999**, *111*, 5221.
(25) Geisinger, T.; Mueller, M.; Binder, K. *J. Chem. Phys.* **1999**, *111*, 5241.
(26) Wang, Q.; Nath, S. K.; Graham, M. D.; Nealey, P. F.; de Pablo, J. J. *J. Chem. Phys.* **2000**, *112*, 9996.
(27) Miao, B.; Yan, D.; Han, C. C.; Shi, A. C. *J. Chem. Phys.* **2006**, *124*, 144902.
(28) Matsen, M. W. *J. Phys. Cond. Matter* **1997**, *14*, R21.
(29) Binder, K. *Adv. Polym. Sci.* **1994**, *112*, 181.
(30) Vassiliev, O. N.; Matsen, M. W. *J. Chem. Phys.* **2003**, *118*, 7700.
(31) Leibler, L. *Macromolecules* **1980**, *13*, 1602.
(32) Fredrickson, G. H.; Helfand, E. *J. Chem. Phys.* **1987**, *87*, 697.
(33) Bates, F. S.; Fredrickson, G. H. *Annu. Phys. Rev. Chem.* **1990**, *41*, 585.
(34) Fredrickson, G. H.; Ganesan, V.; Drolet, F. *Macromolecules* **2002**, *35*, 16.
(35) Fredrickson, G. H. *The Equilibrium Theory of Inhomogeneous Polymers*; Oxford University Press: Oxford, England, 2006.
(36) Ganesan, V.; Fredrickson, G. F. *Europhys. Lett.* **2001**, *6*, 814.
(37) Tsori, Y.; Andelman *J. Inter. Sci.* **2003**, *11*, 259.
(38) Wang, Q.; Nealey, P. F.; de Pablo, J. J. *Macromolecules* **2001**, *34*, 3458.
(39) Mansky, P.; Rusell, T. P.; Hawker, C. J.; Mays, J.; Cook, D. C.; Satija, C. K. *Phys. Rev. Lett.* **1992**, *68*, 67.
(40) Tang, W. H.; Witten, T. *Macromolecules* **1998**, *31*, 3130.
(41) Yin, Y.; Sun, P.; Chen, T.; Li, B.; Jin, Q.; Ding, D.; Shi, A. C. *Chemphyschem* **2004**, *5*, 540.
(42) Brazovskii, S. A. *JETP* **1975**, *41*, 85.
(43) Nie, Z.; Su, Z.; Sun, Z.; Shi, T.; An, L. *Macro. Theory Simul.* **2005**, *14*, 463.
(44) Matsen, M. W.; Schick, M. *Phys. Rev. Lett.* **1994**, *72*, 2660.
(45) Busch, P.; Smilgies, D. M.; Posselt, D.; Kremer, F.; Papadakis, C. M. *Macromol. Chem. Phys.* **2003**, *204*, F18.
(46) Papadakis, C. M.; Busch, P.; Posselt, D.; Smilgies, D. M. *Adv. Solid State Phys.* **2004**, *44*, 327.
(47) Duechs, D.; Ganesan, V.; Fredrickson, G. H.; Schmid, F. *Macromolecules* **2003**, *36*, 9237.
(48) Notice that this is not the original constraint $\hat{\rho}_+(\mathbf{r}) = \rho_o$, or $\hat{\phi}_+(\mathbf{r}) = 1$.
(49) Ceniceros, H.; Fredrickson, G. H. *Multiscale Mod. Simul.* **2004**, *2*, 462.

(50) Wu, D. T.; Fredrickson, G. H.; Carton, J.-P.; Ajdari, A.; Leibler, L. *J. Polym. Sci., Part B: Polym. Phys.* **1995**, *33*, 2373.
(51) Wu, D. T.; Fredrickson, G. H.; Carton, J.-P. *J. Chem. Phys.* **1996**, *104*, 6387.
(52) Rasmussen and Kalosakas *J. Polym. Sci., Part B: Polym. Phys.* **2002**, *40*, 1777.
(53) Alexander-Katz, A.; Moreira, A. G.; Sides, S. W.; Fredrickson, G. H. *J. Chem. Phys.* **2005**, *104*, 249902.
(54) Knoll, A.; Magerle, R.; Krausch, G. *J. Chem. Phys.* **2004**, *120*, 1105.
(55) Horvat, A.; Lyakhova, K. S.; Sevink, G. J. A.; Zvelindovsky, A. V.; Magerle, R. *J. Chem. Phys.* **2004**, *120*, 1117.
(56) Alexander-Katz, A. Ph.D. Thesis 2004.
(57) Alexander-Katz, A.; Moreira, A. G.; Fredrickson, G. H. *J. Chem. Phys.* **2003**, 11*8*, 9030.

MA070005H